Acousto-Optical Tunable Filter Atmospheric Imager for Determination of Aerosol Extinction

Brenden J Elash, Adam E Bourassa, Douglas A Degenstein

April 17, 2015

1   Introduction

The Atmospheric Limb Imager (ALI) is a prototype atmospheric instrument developed at the University of Saskatchewan with the long term goal for a satellite instrument to gather high resolution horizontal and vertical aerosol microphysics profiles, including extinction and particle size. The purpose of the ALI prototype is to test and verify the use of an Acousto-Optical Tunable Filter (AOTF), the fundamental technology behind ALI, in a space environment and to gather atmospheric sulfate aerosol profiles with high spacial resolution. ALI will measure light from the atmosphere through the limb geometry which measures the radiance from scattered sunlight from sunlit atmosphere. ALI is a single channel instrument measuring radiance from the visible to the near infrared wavelengths (650-950 nm) and through successive images builds spectral information. The system uses a telescoptic front end to pass collimated light through the AOTF which is then focused onto the the detector. The AOTF has the unique property of separating the incoming radiance into each of its linear polarized components and rotating the the selected wavelength polarization by 90° allowing one to recover some polarization information of the incoming radiance. The ALI prototype was completed in August of 2014 and a stratospheric balloon test flight from the Canadian Space Agency (CSA) balloon launch facility in Timmins, Ontario onboard the CNES gondola platform occurred on September 20, 2014.

The atmosphere has been monitored in several different geometries throughout history. Occultation was one of the first methods used on satellite instrumentation to measure atmospheric species, including ozone. Notable instruments included SAM II (*McCormick et al.*, 1979), SAGE II (*McCormick*, 1987), and SAGE III (*Thomason and Taha*, 2003). Different instrumentation techniques were also put into space to acquire atmospheric data for different species with differing resolutions and quantity of data that could be acquired in a single day. One such geometry is the limb scatter geometry which measures radiance from the sunlite atmosphere as it scatters and interacts with molecules. However, the limb scatter geometry has a complexity that requires a foreword model to be able to accurately compute the scattering interactions, both single and multiple, between different constituents in order to be able to acquire any useful atmospheric information from the recorded data. Two instruments from the previous generation of remote sensing instruments have successfully used limb scatter to determine atmospheric parameters, the Optical Spectrograph and InfraRed Imaging System (OSIRIS) an Canadian instrument onboard the Odin satellite (*Llewellyn et al.*, 2004) and SCanning Imaging Absorption spectroMeter for Atmospheric CHartographY (SCIA-MACHY) onboard the ENVISAT (*Bovensmann et al.*, 1999) which are grating spectrometers that can only acquire data at a single altitude at a time so a series of exposures is required to create a vertical profile with approximately a 2 km sampling rate. The new proposed method with ALI allows for two dimensional spacial images of a single wavelength with polarized light to be acquired giving both vertical and horizontal resolution of the environment through the use of the innovative AOTF technology.

Sulfuric aerosol is a fundamental portion of the global climate balance. Work by *Andreae et al.* (2005) has shown that global warming has not been as drastic as perviously expected due to the high amounts of aerosol in the stratosphere currently due to the high volcanic activity. Aerosol is a spherical partial that scatteres incoming radiance away from the surface of the planet causing an overall cooling effect which is dependant on particle size distribution (*Kiehl and Briegleb*, 1993). This effect is fully defined by aerosol microphysics requiring accurate knowledge of concentration and particle size distributions. Furthermore, high resolution aerosol measurements are required in order to be able to determine aerosol extinction ratios during high aerosol loading due to the long path length and high amounts of scattering. The method of aerosol transportation across the tropopause are not completely understood, recently after the 2011 eruption of Nabro it was determined that

the asian monsoon has the ability to penetrate through the thermal boundary and ejected aerosol from the Nabro plume into the stratosphere (*Bourassa et al.*, 2012). Current generation instrumentation does not have the necessary resolution needed for current scientific needs and additional horizontal and vertical resolution will allow the determination of aerosol loading from volcanic and anthropogenic sources causing a cooling effect and account for losses from the stratosphere due to transportation that will counteract the previous cooling effect. ALI, a prototype for a next generation of instruments will address the much needed horizontal and vertical resolution improvement required to help answer questions about global climate.

In this paper the first section will outline the technology behind the AOTF used within the ALI system and then describe the optical design behind ALI including an ulterior optical presentation including the comparison with the Belgium instrument ALTIUS. Followed by ALI's maiden flight onboard the CNES CARMEN gondola from the CSA balloon launch facility in Timmins, Ontario including the conditions and trajectory of the flight, and the measurements taken during the campaign including an analysis of the conversion from raw measurements into calibrated data. Lastly, an retrieval algorithm for aerosol extinction and particle size parameters will be outlined and then preformed on the data from the campaign.

2 Instrument Design

2.1 Acouto-Optical Tunable Filter

The use of an AOTF for an image system has several distinct advantages due to its low mass, fast stabilization times of a few microseconds, and no moving parts and has only recently become possible thanks to improvements to non-collinear acosto devices with the use of birefringent materials with large apertures (*Chang*, 1974; *Voloshinov et al.*, 2007) which allowed for the ability to image with AOTF technology. In order for the AOTF to allow the filtering of a specific wavelength a momentum matching criteria must be held where the wave vectors of the acoustic wave match the difference of the incoming and diffracted light wave vectors and can be seen demonstrated in Figure 1. This condition is known as the Bragg matching criteria and is given by

$$\mathbf{k}_i = \boldsymbol{\kappa} + \mathbf{k}_d \tag{1}$$

3

where $k_i = \frac{2\pi n_i}{\lambda}$ is the momentum of the incoming light, $k_d = \frac{2\pi n_d}{\lambda}$ is the momentum of the diffracted light, and $\kappa = \frac{2\pi f}{\nu}$ is the momentum of the acousto wave. The parameters λ, f, and ν are the wavelength in vacuum, the frequency of the Radio Frequency (RF) wave, and the phase velocity in the acoustic medium. The condition given in Equation 1 and the wave vector diagram gives the following relation for a birefringent material undergoing Bragg diffraction

$$\lambda = \frac{\Delta n \nu}{F} \frac{\sin^2(\theta_i + \alpha)}{\sin \theta_i}. \tag{2}$$

Also, through the described interaction the diffracted light goes though a 90° rotation in polarization (*Voloshinov*, 1996). Lastly, a wide aperture is required for an AOTF used for imaging purposes. These devices have been developed (*Gass and Sambles*, 1991) and are currently readily available for imaging purposes.

In order to be able to preform the required spectral imaging a large aperture imaging quality ATOF was acquired from Brimrose of America. It is optically tuned for a range of 600 nm to 1200 nm and made from a Tellurium Dioxide (TeO_2), a birefringent crystal. The extraordinary light is diffracted at 2.7 degrees off of the optical axis of the device. In order to achieve a constant diffraction angle of the first order beam a wedge is attached to the exit aperture of the AOTF to compensate for the angular change that occurs from altering the wavelength. A characterization of the AOTF follows.

Images were taken at a set of RFs spaced every 150 kHz from 160 MHz to 75 MHz and the spectral images were recorded with an HORIBA I320 spectrometer with the minimum FWHM of the spectrometer being 1.175 nm, which is well below the minimum FWHM of the AOTF listed specifications at 1.6 nm. For each RF frequency all of the rows of the CCD are summed together to get the total count measurement at each wavelength. The maximum value of each image is taken to be the diffracted wavelength through the AOTF at each respective RF. A typical spectral measurement result can be seen in the top left panel of Figure 2.

The maximum values from each of the images were determined as well as the wavelengths these values occur. It was noted that the curve appears to follow a power function of the form

$$F = a\lambda^b. \tag{3}$$

A linear least squares fit was preformed in log space finding the coefficients a and b. The fit was performed and appeared to match the data quite well

but a relative error analysis was preformed and it was seen that there was a only an agreement better than 0.6% within the testing range and would increase for wavelengths outside the testing region. A better fit was desired to characterize the AOTF's RF-spectral dependance so a modified power function was used in the form of

$$F = a\lambda^{b+c\log\lambda} \tag{4}$$

or a quadratic least squares fit. These results can be seen in the bottom half of Figure 2. The agreement of this form is less than 0.1% throughout the whole wavelength range and the determined RF and wavelength relation can be seen in

$$F = \exp{(19.793)}\lambda^{-3.381+0.168\log\lambda}. \tag{5}$$

It should be noted that even though the AOTF optical range is 600 nm to 1200 nm this analysis only measures wavelengths from 600 nm to 950 nm. The low quantum efficiency of the CCD and the low near IR emitted from the light source causes wavelengths past this point to be noisy.

The same set of data was used to determine the FWHM for each of the above determined wavelengths. The results of this study are shown in the top right of Figure 2. Wavelengths past approximately 1080 nm are to noisy too be able to determine the FWHM of the signal which is not a problem since ALI only measures light out to 950 nm. However, the AOTF spectral resolution is well within the limits that are required in order to determine aerosol extinction in the upper troposphere and lower stratosphere.

2.2   Optical Design and Performances

The AOTF limits the optical system to only have two practical layouts since the incoming light must enter the device at less than the acceptance angle. This is the maximum angle light can enter the device and still undergo the diffraction interaction. These two layouts are a telecentric and a telescopic system. The telescope or afocal system causes a wavelength gradient to be formed across the field of view of the image whereas the telecentric design overcomes this problem but has a larger FWHM (*Suhre et al.*, 2004).

A telecentric layout in both image and object space has an advantage for the imaging quality of the AOTF system. Since the wavelength filtered by the AOTF is dependant on the incident angle, all the lines of sight enter with approximately the same angular spread so the filtered image has consistent

central wavelength with a larger spectral FWHM since the diffracted wavelength is dependance on incident angle as seen in Equation 2. This system does have two inherent issues. First, this method is sensitive to any surface defects of the crystal since the light enters the crystal in focused bundles. Second, a blurring effect is added to the final image that is dependant on wavelength.

The blurring effect is caused by the inherent change of optical path length. First, the optical path between the first two lenes is a fixed distance, however the AOTF is made of TeO_2 or paratellurite and has a high index of refraction of 2.43 and 2.27 for the extraordinary and ordinary optical axes respectively. The crystal also has a high dispersive property, or Abbe number, so the index of refraction depends on the wavelength. The dispersive nature gives an apparent change in the optical path. The change in path length, d, is given by

$$d = \frac{n(\lambda) - 1}{n(\lambda)} t \tag{6}$$

where $n(\lambda)$ is the index of refraction with a wavelength dependance and t is the thickness of the crystal. The AOTF crystal causes the optical path in air to be lengthened by d. In order to compensate, the length d must be added to the path to account to the discrepancy, but this can only be accounted for a specific wavelength due to the high dispersive nature and thus defocusing will occur at the image plane for other wavelengths. In order to correct for this problem additional compensating optics would need to be added or the CCD would need to be actively moved as the wavelengths are being scanned.

In the telescoptic system the AOTF has collimated light passing through the device and this has a few fundamental changes that alter to the system's imaging quality. First, the primary light passing through the AOTF from a single line of sight enters the AOTF at the same angle, so the image will have a smaller FWHM than the telecentric counterpart. However, each line of sight will be diffracted with a different fundamental wavelength due to the angular dependance in the AOTF Bragg diffraction wavelength equation (Equation 2). The final image has a smaller spectral bandpass but there will be a wavelength gradient radiating out from the center of the image. Second, since light now passes through the AOTF collimated, the focal point of the image no longer changes with wavelength. Instead a lateral displacement of each line of sight occurs based on the angle of incidence and the diffracted wavelength which causes a slight magnification of the image. The lateral

6

displacement that occurs is given by the following relation

$$\delta = (n(\lambda) - 1)\frac{t\theta}{n(\lambda)} \tag{7}$$

where δ is the displacement from the original path, but this magnification is a negligible change overall.

The telescopic system offers the ability of having an image plane location that is not dependant on the wavelength being imaged and was the ultimate optical choice for ALI. A telecentric system would lead to a system that would either require mechanical components to move the imaging plane or additional optical elements to counter act the change in the optical path. Using mechanic components to move the camera would be an addition failure point and would have to be well calibrated across the wavelength range. For the other alternative a custom lens or prism would need to be created in order to counteract the defocusing effect of the AOTF which would cause further reflections within the system increasing the possibility of significant stray light hitting the CCD camera and well at decreasing the signal throughput. The telescopic design would also allows for a greater focus on spacial resolution that could be achieved which is necessary in order to be able to image the fine structure of aerosol extinction on the order of 100s of metres.

Another minor consideration for the system is the narrower FWHM for each line of sight that passes through the ATOF and is imaged on the QSI 616s CCD giving finer spectral resolution however the draw back is that the central wavelength of each line of sight is dependant upon the angle of incident. A wavelength gradient appears in the final image. The longest central wavelength occurs in the center of the image and radiates outward towards shorter wavelengths as apparent in Equation 2. Using the telescoptic layout ALI would have a wavelength gradient of approximately 7 nm at 650 nm central wavelength and 11 nm at 950 nm, however for a space based instrument with a relatively smaller field of view the gradient could be reduced to as small as 2 nm across the whole image which, at worse, slightly larger than the FWHM of the AOTF. This effect would be a significant problem for instruments measuring trace gasses absorbtion lines, for example water vapour, but aerosol is a broadband enhancing feature in which its effects are visible in atmospheric measurements from 500 nm well into the IR. The wavelength dependant magnification mentioned earlier only amounts to being a change of a approximately 4 pixels or 0.4% in both directions from the inherent magnification from 650 nm to 950 nm and overall this change is

considered negligible. The final optical specification for ALI can be found in Table 1.

Effective focal length (mm)	74.3
Front optics magnification	0.67
Back optics magnification	1.27
Field of view (°)	6.0 x 6.0
F-number	7.5
Image Size (mm)	9x9
Spectral Range (nm)	650-950

Table 1: ALI Final System Optical Parameters.

ALTIUS, a Belgium instrument, uses similar technology as ALI except uses a telecentric optical layout and is designed to measure atmospheric trace gases (*Dekemper et al.*, 2012). Trace gases have narrow absorbtion and emission features that require specific wavelength knowledge. A telecentric layout will give a of constant wavelength across the whole field of view to be able to be able to resolve absorbtion features. The optical specifications are similar between the two instruments, however two key differences will be noted. First, the field of view of ALTIUS is smaller at 5.73x5.73° and if ALI would have used a telecentric design then it would have had an identical field of view due to the geometry and optical requirements of the telecentric layout. In a telecentric design the AOTF aperture directly limits your instruments field of view and both systems use an ATOF crystal with an optical aperture of 10x10 mm. Second, the f/# for ALTIUS is 14.32 compared to ALI's 7.5 which allows ALI to increase light throughput at the cost of slightly higher abberations in the final image.

3   Stratospheric Balloon Flight

3.1   Flight Day Conditions and Flight Path

The balloon launch base in Timmins, Ontario is located at 48.4667°N 81.3333°W and ALI arrived at the base on August 28, 2014 with a launch window from September 8 to 14, 2014. In between the arrival and launch ALI needed to be integrated onto the CARMEN gondola and verify no conflicts or problems

with CARMEN's systems, including communications and power. ALI was orientated so it would be 90° from the direction of the sun in regard to the gondolas pointing system with an overall southern field of view during the mission.

The flight of CARMEN was delayed due to poor weather conditions during the launch window. On September 20, 2014 at 05:35 UTC (01:35 local time) ALI was launched as the Nimbus 7 mission onboard the CNES CARMEN gondola from the CSA Timmins balloon launch facility. During the launch, the sky was clear with light winds allowing for an safe and uneventful launch. The ascent of CARMEN occurred in darkness and reached its flight altitude of 36.5 km at 8:17 UTC. First light was observed by ALI at 9:39 UTC and recorded measurements until 14:42 UTC when the primary aerosol mission was completed. ALI was powered off at 17:15 UTC during this time ALI recorded measurement for secondary goals, including an azimuth scan. A visualization of the flight path with all major landmarks noted can be found on Figure 4. During the mission, an operational mode for aerosol was ran that gathered images from 650-950 nm with 25 nm separation approximately every 25 s.

3.2   Measurements

The inherent nature of a AOTF based instrument results in only a specific polarization of radiance being measured by the device. The AOTF transmits light entering the AOTF vertically polarized from the front face of the AOTF in the factory specified orientation, which is identical to its orientation within ALI. ALI measured light that is polarized 90° from the horizon or what is known as the vertical polarization. This resulted in a system where ALI only measured 10 to 35% of the total incoming radiance due to the polarization and requires a radiative model that can accurately compute polarization radiances.

The raw flight data (level 0) must be converted to relative radiances (level 1) before they can be used to retrieve aerosol extinctions and particle sizes. The transformation includes removal of dark current, the DC bias, stray light, and flat fielding. Using the dark images from the assent of the flight combined with laboratory dark test images a table of values based on exposure time and CCD temperature was computed to be able to remove the DC bias and dark current from each raw image accurately. Once completed, the constant offset caused by the DC bias allows for the rest of the analysis

9

to be preformed in counts per second, by taking the counts in the image and divided by the exposure time, in order to easily relate the radiance of different images directly to each other without having to scale the results with respect to the exposure time.

Stray light removal has always been difficult in atmospheric instrumentation due to the difficulty in accurately discerning the signal in regards to the stray light containmination. Furthermore, ALI's optical system has the further addition of unwanted light internal to the instrument because of the rejection of one of the polarizations due to the nature of the AOTF. The signal enters the optical system unpolarized, but the AOTF only operates on one polarization. The entering light is passed through a linear polarizer with an extinction ratio of at least 100,000:1 to remove the unwanted polarization however a small percentage is not absorbed. Furthermore, a second linear polarizer is used after the AOTF to reject all of the unwanted radiance that did not meet the Bragg criteria and once again a small percentage of this radiance is not absorbed. The active filtering of the AOTF allows for an image to be measured when the filtering device is disabled allowing only the stray light to be captured by the measurement known as a 'dark image', and during ALI's aerosol mode a 'dark image' was captured before every measurement image. By removing the 'dark images' from the signal-stray light contaminated images the end result is images that only contain the measured signal. The previous method was tested in the lab with a known source with even illumination across the field of view of the system, the resulting final image is left with a even decrease in intensity radiating from the center of the field of view as its expected with the known vignetting of ALI.

To finalized the data into level 1 relative radiances a flat fielding calibration is underwent. The flat fielding coefficients needed to be applied not only spacially across each image but spectrally as well. To determine the flat fielding coefficients ALI was set up in the lab viewing the light emitted from a quartz-tungsten halogen bulb that is passed through a diffusing plate to give an even laminar radiance across the entire field of view of ALI. Several series of measurements were taken at varying integration times at wavelengths the same as ALI's aerosol mode and used to normalized the full field of view across the whole spectrum to the center of the 750 nm images, thus giving a relative calibration of radiance referenced to this point. The process used to determine the flat fielding coefficients started with similar process used to remove the stray light during the mission post processing. The images had the DC bias and dark current removed for proper unbiased comparisons and

converted to counts per second. Each value of every pixel in the active region of the CCD was normalized to the mean of the value on the center 25 by 25 pixels at 750 nm over all exposure times and trials. The coefficients for flat fielding can be determined as the values to yield a unified radiances of one across all field of views and wavelengths. These coefficients are then applied to the data from the flight that give relative radiances for each pixel.

To increase the precision of the measurements from the flight the images were averaged in cells of 25 horizontal and 10 vertical pixels decreasing the resolution to 9.2 by 3.7 arcminutes but greatly reduces the error on the radiances. Furthermore, a loss of resolution was also noted in the flight data and is caused by the drastic change in temperature of the optics during the flight which is a secondary reason for the pixel averaging. A large number of vertical profiles with a horizontal dependance are determined from the new radiance vectors. The final relative radiances can be seen in Figure 5.

3.3   Retrievals

The modeled radiances were computed with the SASKTRAN radiative transfer engine (*Bourassa et al.*, 2008) for for High Resolution (SASKTRAN-HR) (*Zawada et al.*, 2015) measurements using the newly developed polarization module. The model uses a given atmospheric state to solve the radiative transfer equation to determine the final radiance at the observer that follows

$$I(s_1) = I(s_0)e^{-\tau(s_0,s_1)} + \int_{s_0}^{s_1} k(s)J(s)e^{-\tau(s,s_1)}ds \tag{8}$$

where $I(s_1)$ is the radiance at the observer through a path from s_0 to s_1, the first term is the contribution of light that is attenuated along the line of sight from the sun to the observer at s_1. The second term takes the source term, $J(s)$, which is the radiance scattered into the line of sight and integrates the path along line of sight with attenuation to determine the scattering contribution to the final radiance. The extinction, given by $k(s)$, is the sum of the number density, $n(s)$, multiplied by the cross section, $\sigma(s)$, over all species. The polarized output of SASKTRAN-HR gives the stokes vectors for the radiance on its internal coordinate grid which can be retrieved from the model and then can be rotated to match ALI's coordinate system.

The relative radiance level 1 data from ALI are used create a measurement

11

vectors, y, from the data in the following form

$$\mathbf{y} = \frac{I(\mathbf{z}, \lambda)}{I(z_{ref}, \lambda)} - \frac{I_{rayliegh}(\mathbf{z}, \lambda)}{I_{rayliegh}(z_{ref}, \lambda)} \tag{9}$$

where $I(z, \lambda)$ is the measured radiance from ALI and $I(z_{ref}, \lambda)$ is a reference altitude used to normalize the signal from a high altitude where there is little aerosol contribution, for ALI the highest possible altitude where the signal is above the noise threshold is around 26-30 km tangent height which brings out the aerosol signal in the vector. The second term is modeled values from SASKTRAN-HR with only background neutral atmosphere to remove the rayleigh signal form the measured radiances which is done to improve the speed of the convergence of the retrieval. A base aerosol state or a priori, $\mathbf{x}$, for aerosol extinction profile is used in the SASKTRAN-HR model. The foreword model vector is constructed similarity to the measurement vector and follows.

$$\mathbf{F}(\mathbf{x}) = \frac{I_{mod}(\mathbf{z}, \lambda)}{I_{mod}(z_{ref}, \lambda)} - \frac{I_{rayliegh}(\mathbf{z}, \lambda)}{I_{rayliegh}(z_{ref}, \lambda)} \tag{10}$$

where $I_{mod}(z, \lambda)$ is the modeled radiance for the measurement and $I_{mod}(z_{ref}, \lambda)$ is the measurement at the same reference altitude for normalization. The foreword model is used in combination with the measurement vector to update the extinction profile in the Multiplicative Algebraic Reconstruction Technique (MART) algorithm with the following iterative technique

$$x_{i+1} = x_x \sum_j \frac{y_j}{F(z_j)} W_{ij} \tag{11}$$

where i is the aerosol extinction at each measurement altitude and j is the tangent point internal to the SASTRAN model, know as the shell altitudes. W_{ij} is the weighting matrix that relates the tangent altitudes to the shell altitudes. This method was outlined by *Degenstein et al.* (2009) and allows for fast retrievals without calculating a Jacobian.

An error estimation was also needed to be able to fully classify the capabilities of ALI and was performed using a perturbation method. Once a retrieval has been completed for an image the result is used to estimate the error in the returned extinction. For each altitude, the measurement vector is perturbed by the error resulting form the level 0 to level 1 data conversation and from the readout electronics. The MART retrieval is rerun and the change of the extinction is determined. These are compiled to form a

Jacobian, $\mathbf{K}$, with size is n by m which are the shell altitudes and the tangent altitudes grids respectively. The error at each retired altitude is then given by

$$\mathbf{e} = \left(\mathbf{K_{ij}K_{ji}^{-1}}\right)^{0.5} \tag{12}$$

which gives the error at at retrieved altitude.

Once the retrieval has been preformed for a complete series of wavelengths a determination for the angstrom exponent occurs which is preformed in a similar manor as outlined by *Rault and Loughman* (2013). Since the measurements observe relatively the same atmosphere over the time of one complete aerosol cycle; the differences between extinction ratios at the different wavelength can be used to gather a understanding of aerosol particle size in the form

$$\frac{n\sigma}{n_0\sigma_0} = \left(\frac{\lambda}{\lambda_0}\right)^{-\alpha} \tag{13}$$

where n is the aerosol concentration, σ is the cross section, and α is the angstrom exponent. Since the cross section of aerosol is dependant on not only the wavelength but also the particle size and distribution the angstrom coefficients give some information on particle size. For the retrieval described here a single mode log-normal distribution is assumed with a mode radius, r_g, and the mode width, σ_g which is commonly used for aerosol profiles (*Bingen et al.*, 2004). At each retrieved altitude the extinction from each wavelength is used to fit a line and determine the angstrom coefficient. Then the median value from all the altitudes is used as the new size parameters in next iteration of the retrieval. The mode width would be set at a constant 1.6 and the mode radius is varied to achieve an identical angstrom exponent as retrieved. The mode radius is updated and the process is repeated until the angstrom exponent converges and at the end of the last iteration the angstrom exponent profile is kept unaltered as the final particle size product.

3.4   Results

In order to be able to use the ALI data in the MART method certain quantities were needed for the model; albedo, ozone concentration and cross sections, and aerosol cross sections. The albedo is required since an absolute radiance calibration was never preformed with ALI and the albedo cannot be determined directly form ALI's measurements, which is important since the amount of ground scatter in SASKTRAN-HR must correspond to the ground

scatter during ALI's flight. Second, the ozone absorbtion features from the Chappuis band appear in the ALI measurements from 650 to 750 nm. The absorbtion must be accounted for to not artificially change the determined aerosol profiles. The ozone profiles were acquired from OSIRIS. Five scans that were with 48 hours of the balloon flight and within 500 km of the launch facility were averaged together to be the ozone profile used in the SASKTRAN-HR model, with cross section gathered from the GOME flight instrument done by *Burrows et al.* (1999). The albedo is from the ADAM database which has monthly values for albedo over the surface on earth at a resolution of 0.1° x 0.1° grid at 1 nm spectral resolution (*Muller et al.*, 2013). The aerosol cross sections come from the Mie scattering derivation that was originally proposed by Mie and was implemented efficiently by *Wiscombe* (1980). It is important to note that the scattering direction and cross section of aerosol particles depends on the size distribution so a knowledge of particle size is required for highly accurate aerosol measurements. For the purpose of the retrieval an a priori was used with a mode radius of 0.08 µm and a mode width of 1.6 which is considered a standard size distribution for aerosol (*Deshler et al.*, 2003).

The complete mission consisted of 217 images that were recorded in illuminated conditions and were used in the MART method. The retrieval method was run on the full mission but this paper will focus on a signal set for the purpose of the analysis, specifically the last complete set of images from 650 to 950 nm consisting of images 204-217 will be used. They were chosen due to being the last in the mission and the sun was the highest in the sky giving the brightest atmosphere leading to the best signal to noise during the mission. A sample of the retrieval set can be observed in Figure 6 which highlights the 725, 825, and 925 nm retrievals at 1 km shell resolution. The left panels shows the measurement vector from ALI in black with the foreword model radiance profile from SASKTRAN-HR in blue. For each of the wavelengths, the algorithm determines altitudes where the value of the measurement vector is less than the known noise and does not allow aerosol to be retrieved in those regions. Instead the scaling factor, given by $\alpha = yF^{-1}$ is scaled to the aerosol profile above and below the last retrieved point to keep the aerosol profile smooth, as discontinuities are nonphysical and can lead to a convergence failure in the MART algorithm. The middle panel shows the convergence between the measurement vector and the foreword model result. For the center wavelengths, being 700-875 nm, a different of less than 2% is seen from 12 to 22 km with a few outliers and for the fringe wavelengths this

14

is reduced to better than 3% from 17 to 20 km.

The aerosol profile for the three wavelengths is shown in blue with the shading representing the error for the retrieval strictly based on measurement error and neglecting any model and atmospheric state errors. The green curve is the average 750 nm aerosol extinction profiles of the same five OSIRIS scans used for the ozone profile and red is the 750 nm aerosol extinction from SALOMON (*Berthet et al.*, 2002) which was launched from the Timmins balloon base as the Nimbus 5 mission on September 12, 2014. The aerosol extinction for ALI and OSIRIS are within 50% of each other for a majority of the 725 nm and 825 nm profile while the upper altitude of the 925 nm are considerable different, in some places over 100% difference occurs. SALOMON's extinction profile are considerable larger than ALI's results but it is important to note is that all three instruments follow the same shape for all the profiles. First, a bend in the profile occurs at approximately 25 km, then increases approximately linearly until 15 km where aerosol extinction leaves the linear trend and forms the peak of the measurement. The agreement in shape is an excellent result for the ALI mission due to the good numerical comparison with OSIRIS as well as the overall profile shape agreement between all three instruments.

The particle size method was used as outlined in the pervious section using the angstrom exponent to gather a general idea of the particle size distribution during the ALI mission. The first panel of Figure 7 shows the median angstrom exponent that was determined after each iteration and convergence can be seen after a couple iterations. The particle size determined for ALI in the last complete set of aerosol images can be seen in the second panel of Figure 7 which yields a final angstrom exponent of between 2 at the high altitudes (20 km) and closer to 4 near the peak of the aerosol extinction layer around 12 to 15 km. Assuming a mode width of 1.6 yields a mode radius of 0.12 µm and 0.01 µm respectively.

In order to determine the angstrom coefficient a least squares fit was used for all usable wavelengths at each altitude. A wavelength at a altitude was rejected if the foreword model at that shell altitude was not with 3% of the measurement vector. In the case shown in Figure 7, the 20.5 km shell altitude, only 8 of the 13 possible wavelength contributed to the angstrom exponent.

4   Conclusions and Future Prospects

A description of the prototype ALI using an AOTF for active filtering in the visible to near IR with a telescopic optical layout with the purpose to measure aerosol extinction from the upper troposphere and lower stratosphere with a high vertical and horizontal resolution with monochromatic images was presented here. The AOTF has fast stabilization times and the ability to disable the filter gives an excellent method to remove stray light from the final measurements. ALI is able to measure aerosol microphysics in remote atmospheric sensing.

ALI was tested on board the CARMEN gondola from the balloon launch facility at Timmins, Ontario. Aerosol extinction profiles were determined and had good comparisons to ORISIS and SALOMON in profile shape. The absolute extinction values are different by a large amounts but could be attributed to the large amount of unaccounted systematics in the retrieval algorithm. Overall ALI preformed admirably and verified the use of this technology for future atmospheric remote sensing missions.

Future upgrades to ALI would include the realignment of the optics for flight temperatures to allow for higher resolution measurements and retrievals. Secondly, replacing the CCD currently used on ALI with a camera with a faster readout would allow for a higher quantity of data to be taken by reducing the approximate 25 s readout time down to a smaller time necessary for a satellite missions on the order of 1 s per wavelength.

References

Andreae, M. O., C. D. Jones, and P. M. Cox (2005), Strong present-day aerosol cooling implies a hot future, *Nature*, *435*, 1187–1190.

Berthet, G., J.-B. Renard, C. Brogniez, C. Robert, M. Chartier, and M. Pirre (2002), Optical and physical properties of stratospheric aerosols from bal-

loon measurements in the visible and near-infrared domains. i. analysis of aerosol extinction spectra from the amon and salomon balloonborne spectrometers, *Applied optics*, *41*, 7522–7539.

Bingen, C., D. Fussen, and F. Vanhellemont (2004), A global climatology of stratospheric aerosol size distribution parameters derived from sage ii data over the period 1984–2000: 1. methodology and climatological observations, *Journal of Geophysical Research: Atmospheres (1984–2012)*, *109*.

Bourassa, A. E., D. A. Degenstein, and E. J. Llewellyn (2008), SASKTRAN: A spherical geometry radiative transfer code for efficient estimation of limb scattered sunlight, *Journal of Quantitative Spectroscopy and Radiative Transfer*, *109*, 52–73, doi:10.1016/j.jqsrt.2007.07.007.

Bourassa, A. E., A. Robock, W. J. Randel, T. Deshler, L. A. Rieger, N. D. Lloyd, E. T. Llewellyn, and D. A. Degenstein (2012), Large volcanic aerosol load in the stratosphere linked to asian monsoon transport, *Science*, *337*, 78–81.

Bovensmann, H., J. Burrows, M. Buchwitz, J. Frerick, S. Noël, V. Rozanov, K. Chance, and A. Goede (1999), Sciamachy: Mission objectives and measurement modes, *Journal of the Atmospheric Sciences*, *56*, 127–150.

Burrows, J., A. Richter, A. Dehn, B. Deters, S. Himmelmann, S. Voigt, and J. Orphal (1999), Atmospheric remote-sensing reference data from gome2. temperature-dependent absorption cross sections of o 3 in the 231–794nm range, *Journal of Quantitative Spectroscopy and Radiative Transfer*, *61*, 509–517.

Chang, I. C. (1974), Noncollinear acousto-optic filter with large angular aperture, *Applied Physics Letters*, *25*, 370, doi:10.1063/1.1655512.

Degenstein, D., A. Bourassa, C. Roth, and E. Llewellyn (2009), Limb scatter ozone retrieval from 10 to 60 km using a multiplicative algebraic reconstruction technique, *Atmospheric Chemistry and Physics*, *9*, 6521–6529.

Dekemper, E., N. Loodts, B. V. Opstal, J. Maes, F. Vanhellemont, N. Mateshvili, G. Franssens, D. Pieroux, C. Bingen, C. Robert, L. D. Vos, L. Aballea, and D. Fussen (2012), Tunable acousto-optic spectral imager

for atmospheric composition measurements in the visible spectral domain, *Applied Optics*, *51*, 6259–6267, doi:10.1364/AO.51.006259.

Deshler, T., M. Hervig, D. Hofmann, J. Rosen, and J. Liley (2003), Thirty years of in situ stratospheric aerosol size distribution measurements from laramie, wyoming (41 n), using balloon-borne instruments, *Journal of Geophysical Research: Atmospheres (1984–2012), 108*.

Gass, P. A., and J. R. Sambles (1991), Accurate design of a noncollinear acousto-optic tunable filter, *Optics Letters*, *16*, 429–431, doi:10.1364/OL.16.000429.

Kiehl, J. T., and B. P. Briegleb (1993), The relative roles of sulfate aerosols and greenhouse gases in climate forcing, *Science*, *260*, 311–314, doi:10.1126/science.260.5106.311.

Llewellyn, E., N. D. Lloyd, D. A. Degenstein, R. L. Gattinger, S. V. Petelina, A. E. Bourassa, J. T. Wiensz, E. V. Ivanov, I. C. McDade, B. H. Solheim, J. C. McConnell, C. S. Haley, C. von Savigny, C. E. Sioris, C. A. McLinden, E. Griffioen, J. Kaminski, W. F. J. Evans, E. Puckrin, K. Strong, V. Wehrle, R. H. Hum, D. J. W. Kendall, J. Matsushita, D. P. Murtagh, S. Brohede, J. Stegman, G. Witt, G. Barnes, W. F. Payne, L. Piche, K. Smith, G. Warshaw, D. L. Deslauniers, P. Marchand, E. H. Richardson, R. A. King, I. Wevers, W. McCreath, E. Kyrola, L. Oikarinen, G. W. Leppelmeier, H. Auvinen, G. Megie, A. Hauchecorne, F. Lefevre, J. de La Noe, P. Ricaud, U. Frisk, F. Sjoberg, F. von Scheele, and L. Nordh (2004), The OSIRIS instrument on the Odin spacecraft, *Canadian Journal of Physics*, *82*, 411–422, doi:10.1139/p04-005.

McCormick, M. (1987), Sage ii: an overview, *Advances in space research, 7*, 219–226.

McCormick, M., P. Hamill, W. Chu, T. Swissler, L. McMaster, and T. Pepin (1979), Satellite studies of the stratospheric aerosol, *Bulletin of the American meteorological Society*, *60*, 1038–1046.

Muller, J.-P., P. Lewis, F.-M. Bréon, C. Bacour, I. Price, L. Chaumat, P. Prunet, L. Gonzales, C. Schlundt, M. Vountas, et al. (2013), A surface reflectance database for esas earth observation missions (adam), *Living Planet Symposium*.

18

Rault, D. F., and R. P. Loughman (2013), The omps limb profiler environmental data record algorithm theoretical basis document and expected performance, *Geoscience and Remote Sensing, IEEE Transactions on, 51,* 2505–2527.

Suhre, D. R., L. J. Denes, and N. Gupta (2004), Telecentric confocal optics for aberration correction of acousto-optic tunable filters, *Applied Optics, 43,* 1255–1260, doi:10.1364/AO.43.001255.

Thomason, L. W., and G. Taha (2003), Sage iii aerosol extinction measurements: Initial results, *Geophysical research letters, 30.*

Voloshinov, V. (1996), Spectral and polarization analysis of optical images by means of acousto-optics, *Optics Laser Technology, 28,* 119–127, doi:10.1016/0030-3992(95)00079-8.

Voloshinov, V. B., K. B. Yushkov, and B. B. J. Linde (2007), Improvement in performance of a TeO_2 acousto-optic imaging spectrometer, *Journal of Optics A: Pure and Applied Optics, 9,* 341–347, doi:10.1088/1464-4258/9/4/006.

Wiscombe, W. J. (1980), Improved mie scattering algorithms, *Applied optics, 19,* 1505–1509.

Zawada, D. J., S. R. Dueck, L. A. Rieger, A. E. Bourassa, N. D. Lloyd, and D. A. Degenstein (2015), High resolution and monte carlo additions to the sasktran radiative transfer model, *Atmospheric Measurement Techniques Discussions, 8,* 3357–3397, doi:10.5194/amtd-8-3357-2015.
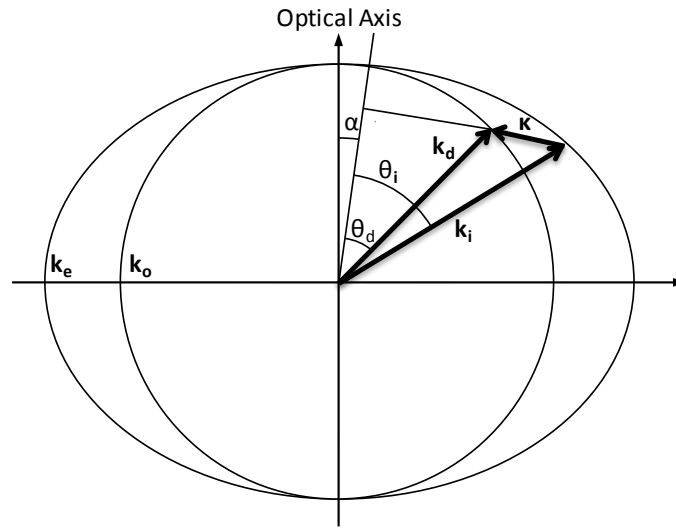
Figure 1: The wave vectors generated by the AOTF experiment. The wave vectors k_e and k_o are for the extraordinary and ordinary axes of the AOTF crystal. The cut angle is shown as α.
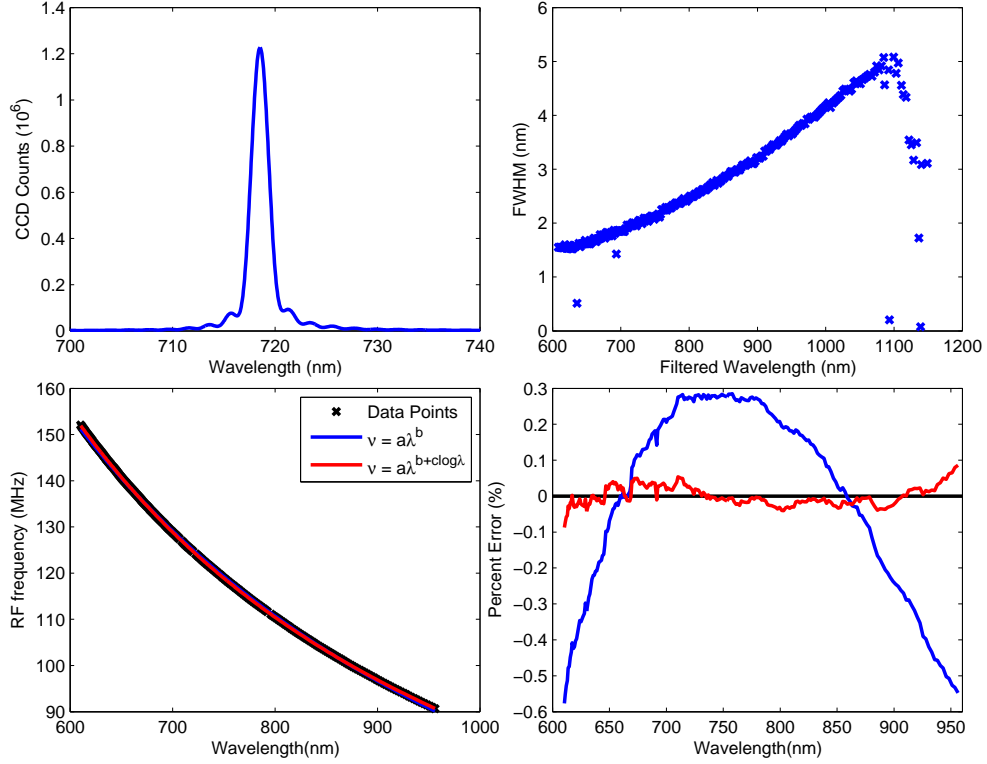
Figure 2: Top Left: A standard image taken from the AOTF calibration experiment when the tuning frequency of the AOTF was at 124.96 MHz. Top Right: The FWHM for each of the determined wavelengths for the AOTF. It should be noted that the FWHM at 600 nm is 1.5 and as the wavelengths get longer the FWHM increases to 4.9 at 1080 nm. Bottom Left: The calibration curves for the AOTF RF versus the diffracted wavelength which contains the data points recorded and two best fit curves. Bottom Right: The percent error with respect to the measured frequency for the two best fit curves in the previous panel.
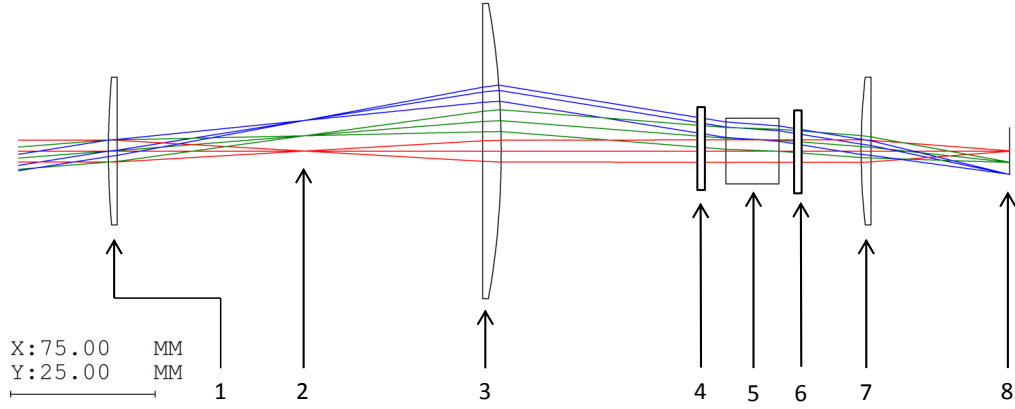
```
X:75.00    MM
Y:25.00    MM
```

Figure 3: Ray Tracing diagram of the telescopic lens system for ALI simulated by Code V optical design software. The elements in the system are the following: (1) 150 mm focal length plano-convex lens. (2) Slit plate. (3) 100 mm focal length plano-convex lens. (4) Vertical linear polarizer. (5) Brimrose AOTF. (6) Horizontal linear polarizer. (7) 50.4 mm focal length plano-convex lens. (8) Imaging plane. It should be noted that the x and y scales are not the same in this image.

Figure 4: The GPS data from ALI during the Nimbus 7 mission generated via Google Earth. The colour of the line represents the absolute speed of the gondola during the mission. Important landmarks are noted on the image. The end of mission represent the end of the primary aerosol mission. No GPS data was collected from ALI after the power down.
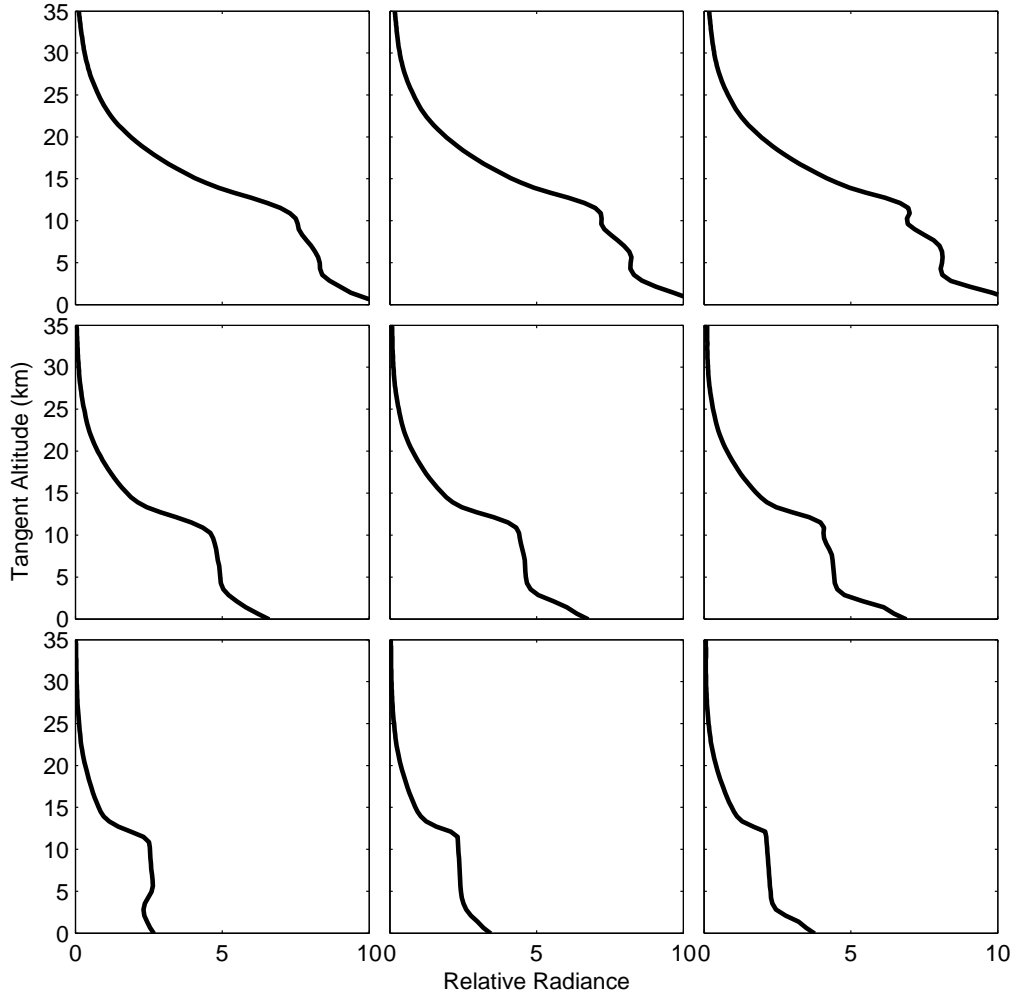
Figure 5: Level 1 relative radiances as measured form ALI at approximately 14:20 UTC (images number 207, 211,and 215) looking 90° from the sun facing southwards. The top middle, and bottom row are measurements taken at 725, 825, and 925 nm respectively. The center column is viewing the atmosphere directly in front of ALI, While the left column is looking to the left at -2.5° and the right at 2.5°.
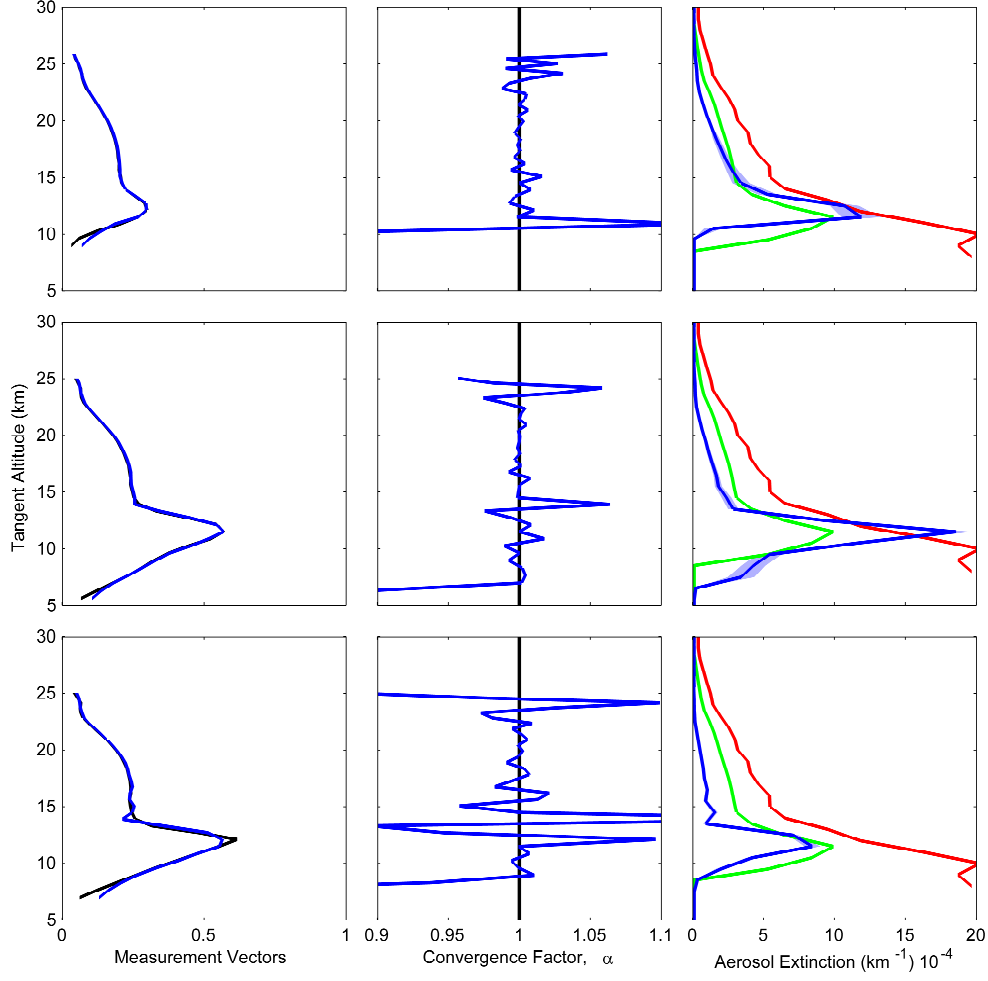
Figure 6: An example of three aerosol retrievals from images 207, 211, and
215, with center wavelengths of 725, 825, and 925 nm respectively and ver-
tically displayed in the figure from top to bottom. The left column shows
the measurement vector, y, in black with the retrieved foreword model, F,
in blue. The center column shows the ratio of the y over F known as α
and is the convergence factor between the ALI measurement and the fore-
word model. The final column is ALI aerosol extinction in blue with the
associated error represented by the light blue shading. The green is aerosol
extinction at 750 nm measured by OSIRIS, and red is 750 nm extinction as
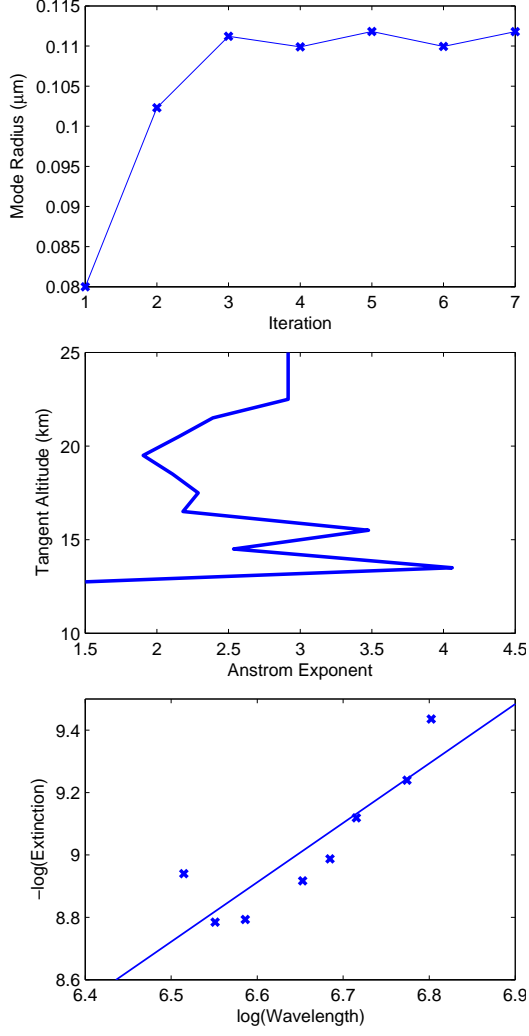measures by SALOMON.

Figure 7: The top panel shows the convergence of the mode radius throughout the iterations in the retrieval. The second panel is the final angstrom exponents determined for images 204-217 during the Timmins 2014 campaign. And the last panel demonstrate a least squares fit to determine the angstrom exponent at 20.5 km shell altitude.